Article

Effects of Defect Density on Optical Properties Using Correlative Cathodoluminescence and Transmission Electron Microscopy Measurements on Identical PrNbO$_4$ Particles

Rasa Changizi, Stefan Zaefferer, Lamya Abdellaoui, and Christina Scheu*

Cite This: https://doi.org/10.1021/acsaelm.2c00253

Read Online

ACCESS | Metrics & More | Article Recommendations | SI Supporting Information

ABSTRACT: Understanding the optical properties of lanthanide niobates is essential to improve the development of these materials. In this study, we investigated PrNbO$_4$ powder particles with different density of twins which influences the intensity of the emission lines. The twins form during synthesis of these particles based on a solid-state route. A correlative approach using backscattered electron imaging, cathodoluminescence measurements, focused ion beam lift out, and aberration-corrected transmission electron microscopy was used at the same location within the particles. Emission lines were acquired by using a cathodoluminescence spectrometer attached to a scanning electron microscope on two regions including twinned and twin free areas. The results were compared and indicate that the areas with higher density of twins have more intense emission lines. The reason for the improved luminescent properties is the perturbation of the energy states caused by the defects which promotes the occurrence of the parity forbidden f−f transitions.

KEYWORDS: *lanthanides, praseodymium niobates, crystal defects, lamellar twins, transmission electron microscopy, cathodoluminescence*
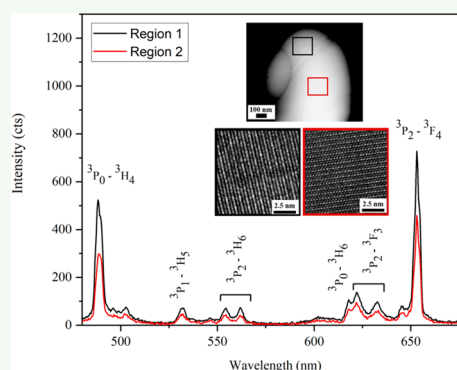
1. INTRODUCTION

Lanthanide niobates have been widely studied in recent decades. The physical properties and chemical stability of these oxides enable them to be potential laser and optical materials.[1−3] A large variety of lanthanide niobates exist with different stoichiometries such as RENbO$_4$, RE$_3$NbO$_7$, RENb$_3$O$_9$, RENb$_5$O$_{14}$, and RENb$_7$O$_{19}$, where RE stands for rare earth lanthanide ions. Based on the RE ions and their ionic radius, different crystal structures exist.[1] According to ref 1 orthoniobates with the formula RENbO$_4$ have enhanced luminescent properties compared to other RE niobates. They crystallize in a monoclinic structure and undergo a reversible ferroelastic phase transformation to a tetragonal system at high temperatures (above 700 °C).[4−6] The transformation temperature depends on the rare-earth ions.[7] Upon cooling, a monoclinic distortion occurs, resulting in the formation of ferroelastic domain structures which resemble twinning.[7,8] This leads to a characteristic ferroelasticity for RENbO$_4$. Ferroelasticity is mainly observed in one of two forms of stress-induced crystal deformations: martensitic transformations and twinning deformation.[9] Both of these deformations are shear-induced and occur without diffusion of the atoms.[9] In the case of martensitic transformations, the crystal structures of the stress-induced domain and mother domain are of different phases, while on the contrary, for twinning deformations the stress-induced domain and mother domain are of the same phase.[9,10]

Different lanthanide niobates have been studied by different groups reporting the presence of twins in their structure, which are briefly summarized here. Prytz and Tafto reported that LaNbO$_4$ shows a phase transformation upon cooling from a tetragonal to a monoclinic structure.[11] Their research indicates that the transformation occurs around 500 °C and causes a monoclinic distortion associated with changes in the lattice parameters. These changes result in an increase in elastic lattice strain, which is accommodated by twinning. The authors referred to these twins as mechanical twins. Other literature reports that for RENbO$_4$ at high temperature the tetragonal scheelite phase is stable, but it reverts to the monoclinic fergusonite phase at ∼550°C upon cooling.[12,13] A series of complex microdomain twins are created due to this phase transition. These microdomains are ferroelastic, and many detailed studies about the domain structures at the nanoscopic regime have been done on them.[8,12−14] Rojas-Gonzalez et al. studied EuNbO$_4$ nanoparticles. By taking high-resolution transmission electron micrcopy (HRTEM) images, they

confirmed the presence of planar defects (twinning) in these particles.[15] Furthermore, they suggested that because of its intense luminescence, the system $LiNbO_3:Eu^{3+}-EuNbO_4$ is a good candidate for building light-emitting devices for medical and biological applications. Fulle et al. used a hydrothermal synthesis approach to grow $RENbO_4$ (RE = La^{3+}, Nd^{3+}, Eu^{3+}, Gd^{3+}, Lu^{3+}).[12] Because of the high vapor pressure during the synthesis, the monoclinic phase directly forms at low temperature without the necessity to form the tetragonal phase first. As a result, twinning is minimized or eliminated, and high-quality single crystals are created.

In our recent work,[16] we compared two types of complex niobates with different praseodymium (Pr) concentration and reported that $PrNbO_4$ with monoclinic structure has enhanced luminescence compared to the cubic $Pr^{3+}:Ca_2Nb_2O_7$. In this study, we focus on $PrNbO_4$ but with the emphasis on its crystal defects (such as twins) and the local differences in defect density to understand the excellent luminescent properties of these materials. We applied a multitechnique correlative methodology and acquired backscattered electron images and cathodoluminescence spectra in a scanning electron microscope (SEM) at identical particles possessing locally different twin densities. (S)TEM lamellae have been prepared by the focused ion beam lift-out technique from the same particles with different density of twins and investigated by using aberration-corrected (S)TEM. We observed that changes in the intensity of the emission lines are related to different defect densities.

2. EXPERIMENTAL PROCEDURES

Synthesis of the polycrystalline samples was done by using a solid-state route with protocols altered from the literature.[17] The optimum amount, described in ref 16, of K_2CO_3, $CaCO_3$, and Nb_2O_5 was mixed together with Pr_6O_{11}. Afterward, to complete the reaction progress, various temperatures between 1100 and 1300 °C were used to anneal the mixture. The product was then washed in deionized water and dried at room temperature. This reaction was done to obtain particles with the nominal formula $Pr_xK_{1-x}Ca_{2-x}Nb_3O_{10}$. X-ray diffraction reported in ref 16 showed the formation of two phases, namely, $Pr^{3+}:Ca_2Nb_2O_7$ and $PrNbO_4$. $PrNbO_4$ particles were produced due to the excess of Pr. For these particles both Ca and K atoms of the parental phase were substituted by Pr. The particles used in the present work are micrometer sized (see SEM images in the following sections).

TEM samples of the $PrNbO_4$ particles were prepared in two different ways. First, electron transparent lamella was prepared by using focused ion beam (FIB) milling from an individual powder particle deposited on a Si substrate. A conventional lift-out technique[18] was performed to prepare the lamella. In the final step, a low-voltage (5 kV) cleaning process was used to remove the surface Ga ions. The entire process was done by using a Scios2 instrument from Thermo Fischer. The lamella was used for bright field (BF) and dark field (DF) TEM imaging as well as diffraction pattern observation and HR(S)TEM studies.

Second, for conventional TEM sample preparation, the powder was mixed with a Gatan G1 epoxy and hardener (two-component glue). The mixture was then put into a brass tube with 2.3 mm inner diameter. After curing the tube at 130 °C, the tube was cut into discs of ~200 μm thickness with a diamond saw. By use of a disc grinder, the discs with a thickness of 80 μm were achieved. To obtain a thickness of 20 μm in the center of the sample, dimple grinding was applied. At the end, a precision argon ion polishing system (PIPS) from Gatan was used to prepare an electron transparent sample.[18] The ion milling was done without sample cooling. This sample was used for TEM observations.

TEM bright field (BF), dark field (DF), and HRTEM imaging as well as selected area electron diffraction (SAED) studies were performed by using a Thermo Fisher Scientific Titan TEM equipped with an X-FEG (field emission gun) as electron source and an aberration corrector for the objective lens. The instrument was operated at 300 kV. Energy dispersive X-ray (EDX) analysis was done by using the attached Super X-detector from Bruker.

Further characterization was performed by using a Thermo Fisher Scientific Titan Themis 300, operated at 300 kV. This microscope is equipped with a C_S probe corrector. For STEM imaging a high angle annular dark-field (HAADF) detector was used. The probe had a convergence angle of 23.8 mrad and a beam diameter of around 0.1 nm.

Cathodoluminescence (CL) data were recorded in a FEG SEM Zeiss SEM 450, equipped with a motorized parabolic mirror (acquisition software Odemis), without a sample cooling system. An electron acceleration voltage of 15 kV, a beam current of 5.5 nA, and a working distance of 15 mm was used. CL images were observed by panchromatic imaging and emission spectra were acquired in spectral mode. Powder particles were mixed in ethanol and dropped on silicon wafers. These wafers were then placed on SEM sample stubs by using copper tape. For the correlative study, the FIB lamella was lifted out from the identical particle on which cathodoluminescence measurements were performed (see Figure S1). Backscattered electron (BSE) images were acquired with the same instrument using 15 kV, a beam current of 2 nA, and working distance of 8 mm.

3. RESULTS AND DISCUSSION

3.1. (S)TEM Analysis of Twins and Twin Densities.

TEM images of $PrNbO_4$ particles exhibit lamellar shape twins as illustrated in Figure 1. Two types of particles with different
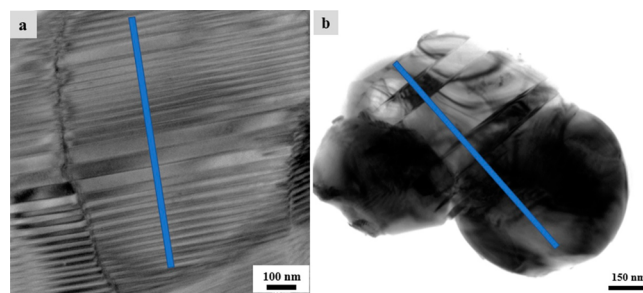
Figure 1. BF images of $PrNbO_4$ particles with (a) higher density of twins (0.05 nm^{-1}) and (b) lower density of twins (0.004 nm^{-1}).

twin boundary densities were observed. Figure 1a shows the BF TEM image of an individual $PrNbO_4$ particle with higher density of twins. The domains vary in size; the smallest observed twin width is less than 20 nm, while the largest observed twin width is more than 50 nm. Another individual $PrNbO_4$ particle with a lower density of twins is displayed in Figure 1b. For this particle, the twin width is slightly larger in size, i.e., 80 nm. As explained in ref 19, when a crystal transfers upon cooling to a structure with lower crystal symmetry, transformation twinning is almost inevitable when the new phase is nucleated at more than one center in the original phase. As stated earlier, these twins show ferroelastic behavior and are induced by stress.[9] Because the free-standing particles did not undergo any external deformation during their production, it must be assumed that the observed twins are due to the phase transformation during the synthesis. To measure the density of the twins, a perpendicular line to the twin boundaries with a length of 900 nm was drawn (indicated with blue in Figure 1). Then the number of twins for each
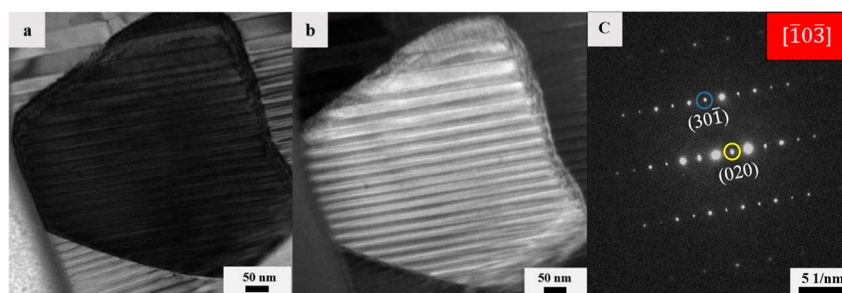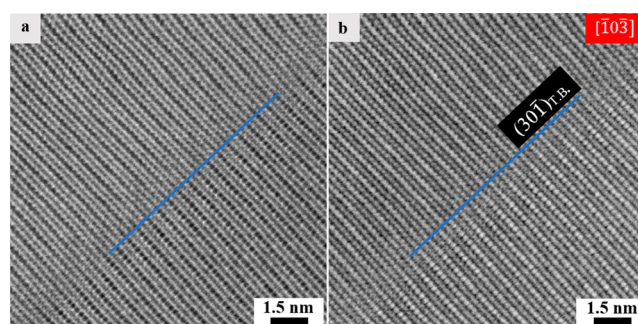
Figure 2. (a) BF image of PrNbO$_4$ lamella with corresponding (b) DF image and (c) SAED pattern in the zone axis $[\bar{1}03]$.

particle was divided by the length of the blue line. The density of the twins for the particles in Figures 1a and 1b was measured by using this line sectioning approach as 0.05 and 0.004 nm^{-1}, respectively.
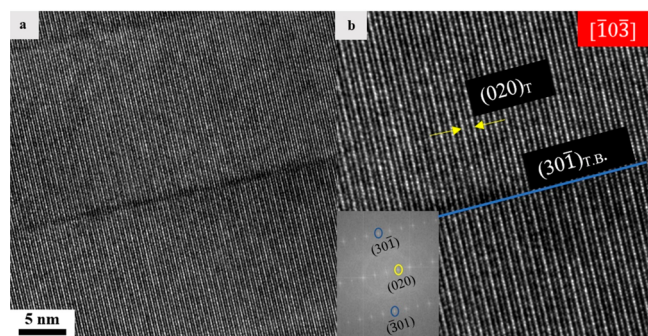
Because the twins with higher density were the dominant type of the observed twins on the particles, further analysis of these twins was carried out. FIB lamella lift out was done on an identical particle on which BSE and CL measurements were performed (see Figure S1). The results of these measurements are given in section 3.2. BF and DF images of the lamella on the same grain are shown in Figures 2a and 2b, respectively. A high density of nanotwins is visible in these images. The corresponding SAED pattern of this grain along the $[\bar{1}03]$ zone axis is given in Figure 2c. The $(3\bar{2}\bar{1})$ and (020) planes are indicated on the diffraction pattern. As shown in the SAED pattern, there are no other phases observed, and the pattern agrees well with the one for PrNbO$_4$ (ICSD109176) which has a monoclinic structure.

To observe the atomic structure, aberration-corrected HRTEM images of the same grain were taken (Figure 3a). A

Figure 3. (a) HRTEM image of PrNbO$_4$ lamella (b) Zoomed-in image on the twins. (T.B. stands for twin boundary). The inset shows the FFT pattern of the same area. Twin boundary is marked with blue circles on the FFT pattern and a blue line on the HRTEM image. Twin planes are indicated with yellow arrows on the HRTEM and a yellow circle on the FFT pattern.

more zoomed-in image is presented in Figure 3b. The inset shows the fast Fourier transform (FFT) pattern which was used to index the twin boundary plane as $(30\bar{1})$. This agrees with Tsunekawa and Takei,[5] who illustrated that $(60\bar{2})$ or $(20\bar{6})$ is a possible twin boundary plane for NdNbO$_4$. The crystal was oriented in the $[\bar{1}03]$ zone axis.

The contrast in HRTEM micrographs cannot be directly interpreted as atomic columns due to the dependence on focus and sample thickness. To confirm where the atomic columns are located, HRSTEM measurements were thus performed on

the same lamella. HAADF and BF imaging of the same grain as shown in Figure 2 are presented in Figure 4. The grain was

Figure 4. (a) HRSTEM-HAADF image of PrNbO$_4$ lamella. (b) HRSTEM-BF image of the lamella in the same location. The blue line on both images indicates the twin boundary plane (both HAADF and BF images are acquired at the identical place).

tilted to the same zone axis as in Figure 3. The twin boundary plane $(30\bar{1})$ is marked with a blue line on both HAADF and BF images. HRSTEM and HRTEM images of the lamella are in agreement with each other. On the basis of that, it is proved that the twins have a coherent structure.

3.2. CL and BSE Analysis of the Twins. To study the influence of the twin density on the optical properties of the particles, CL measurements were done directly on powder particles glued to a support without further sample preparation. BSE imaging was performed to find particles with twins. The results of two particles as the representative of the major group (particles with high density of twins) and minor group (particles with low density of twins) are reported here. Similar analysis of an additional high-density twinned particle can be found in Figure S2. Figure 5a shows BSE image of a PrNbO$_4$ particle (particle I). A high density of twins is seen on this particle. Using the FIB technique, we were able to lift out a lamella from the twinned region of this particle in the upper region. TEM and STEM studies explained in the previous sections were performed on the same lamella. The corresponding panchromatic CL image of the particle is shown in Figure 5b.

Figure 6a illustrates the BSE image taken from another particle (particle II) with a lower twin density. Figure 6b displays the panchromatic CL image of particle II. The density of the twins for particles I and II was measured as explained in section 3.1. The findings are 0.0425 and 0.0075 nm^{-1}, respectively. As we do not observe any intensity difference based on panchromatic CL images, further analysis based on the CL spectra was carried out. As seen in Figures 5a and 6a,
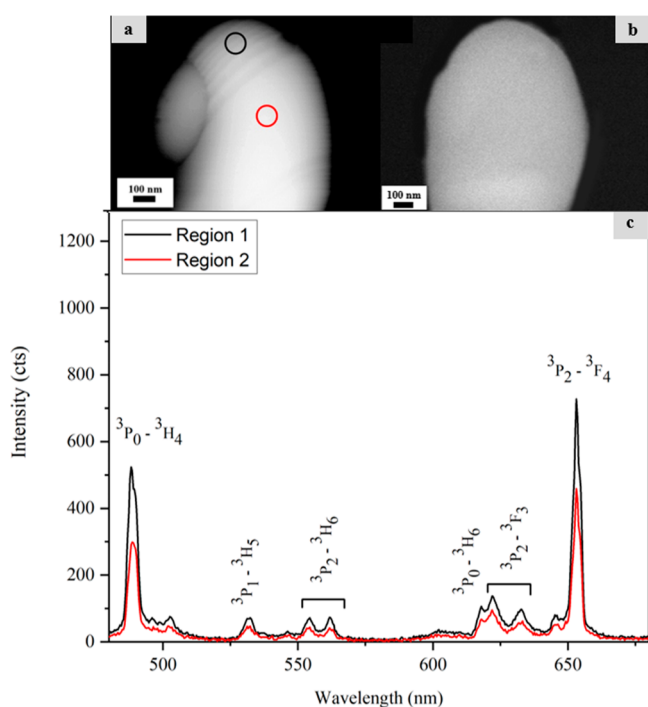
Figure 5. (a) BSE image of the higher density twinned particle (twin density is 0.0425 nm^{-1}) and (b) corresponding panchromatic CL image. (c) CL spectra of the particle where the black curve corresponds to the spectra acquired at the twinned area and the red curve to the twin-free area.
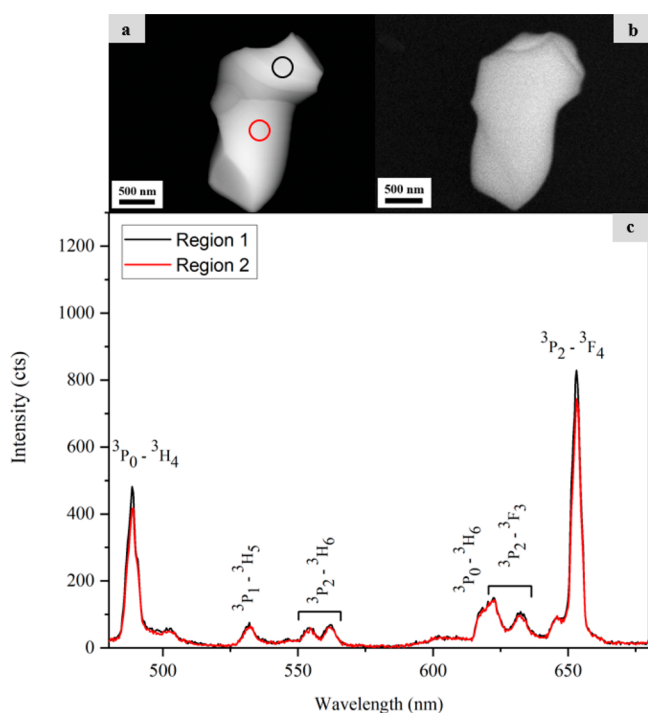
Figure 6. (a) BSE image of a representative particle with a low density of twins (0.0075 nm^{-1}) and (b) panchromatic CL image taken on the same particle. (c) CL spectra of the particle with the measurement areas marked in red (twin-free area) and black (low density of twins) in (a).

not all the regions on the particles have twins. CL spectra for each particle were acquired on the twinned and twin-free areas.

The background noise was removed for all the spectra. The CL spectra of the two selected regions for particle I are shown in Figure 5c. Region 1 is the area with nanotwins of a density 0.0425 nm^{-1}. Region 2 belongs to an area without twinning. Figure 6c displays the CL spectra of two regions for particle II. In both graphs, the twinned areas are colored in black and twin-free areas in red.

The positions of all emission lines are the same in both spectra and exhibit the following transitions: $^3P_0$ to $^3H_4$, $^3P_1$ to $^3H_5$, $^3P_2$ to $^3H_6$, $^3P_0$ to $^3H_6$, $^3P_2$ to $^3F_3$, and $^3P_2$ to $^3F_4$. All these transitions are the main transitions of the lanthanides which are labeled according to the Dieke diagram (Pr^{3+}:$LaCl_3$).[20] However, the intensity is different for the areas with the twins compared to the twin-free area. The intensities of the emission lines are compared to each other and summarized in Table 1.

Table 1. Intensity Comparison between Four Spectra Related to the Twinned and Twin-Free Areas of the Particles

regions	$^3P_0$ to $^3H_4$	$^3P_1$ to $^3H_5$	$^3P_2$ to $^3H_6$	$^3P_0$ to $^3H_6$	$^3P_2$ to $^3F_3$	$^3P_2$ to $^3F_4$
(I) twinned	524	72	73	107	117	728
(I) twin free	297	47	44	64	76	459
(II) twinned	482	66	68	109	129	829
(II) twin-free	416	66	68	109	129	744

For particle I the intensity of the twinned area is considerably higher compared to the twin-free areas. Whereas for particle II, which has lower density of twins, the intensity of the twinned area except for the dominant transitions is the same compared to the twin-free area. To determine the exact difference, we have calculated the relative differences between the twinned versus twin-free peaks with respect to the lower peaks. Results are shown in Table 2.

Table 2. Percentage Difference of the Twinned versus Twin-Free Peaks

particle	$^3P_0$ to $^3H_4$	$^3P_1$ to $^3H_5$	$^3P_2$ to $^3H_6$	$^3P_0$ to $^3H_6$	$^3P_2$ to $^3F_3$	$^3P_2$ to $^3F_4$
(I) % difference of the twins vs twin-free peaks	+76	+53	+66	+67	+54	+58
(II) % difference of the twins vs twin-free peaks	+16	0	0	0	0	+11

We compared the peak ratios and position of the twin-free areas for both particles. Despite having different thicknesses for each particle leading to changes in the absolute intensity values, the relative intensity ratios for all the peaks except $^3p_2$ to $^3F_4$ are similar, and the peak position changes only within 1 nm. These data are given in Table S1.

For particle I, because of the high density of twins, all the peaks show a 53% to 76% increase versus the peaks from the twin-free areas. However, for particle II, only the peaks associated with $^3P_0$ to $^3H_4$ and $^3P_2$ to $^3F_4$ are increased by 16% and 11%, respectively. These two transitions are considered as the dominant transitions of the trivalent Pr regardless of the type of host.[21−26] For the rest of the transitions, no difference was observed. The reason for higher intensities observed for particle I in total could be related to the higher density of the twins. As explained in ref 27, because of the shielding effect of the outer 5s and 5p electrons, the optical properties of inner

shell f−f transitions in lanthanide compounds are usually not sensitive to the surrounding environment. However, there exist exceptional transitions which are called hypersensitive transitions.[28] The intensities of the hypersensitive transitions change greatly by a small change of surrounding environment, although their excitation energies remain insensitive.[28] These transitions obey the selection rules, $|\Delta S| = 0$, $|\Delta L| \leq 2$, and $|\Delta J| \leq 2$ in the case of the Pr^{3+} ion with ΔS being the difference in the spin quantum number, ΔL of the orbital angular momentum, and ΔJ of the total angular momentum.[28] On the basis of this, we know that transition associated with $^3P_2$ to $^3F_4$ is hypersensitive, and this can explain why this transition has higher intensity compared to the rest.

Monte Carlo electron trajectory simulations in $PrNbO_4$ were performed by using the software Casino v2.51 at an acceleration voltage of 10 kV (see Figure S3). The electrons penetrate into the sample up to 500 nm, and the width of the penetration is around 800 nm. Thus, the interaction volume is smaller than the particle size. Although, the CL signal comes from a volume with several hundred nanometers in dimension, we can still distinguish clearly the regions with high twin density and low twin density. It is also important to mention that our TEM investigations reveal that the twins extend from the top surface to the bottom surface of the particle, and thus a large twin area is contributing to the observed CL signal.

The presence of defects in lanthanide-doped materials allows parity-forbidden f−f transitions to occur.[29−31] According to ref 32, local distortions (surface effects and defects such as vacancies, dislocations, and interstitial defects) will lower the symmetry and therefore induce an increase in the relative intensity of the electric dipole transitions. Similar effects are also expected for twins. Because higher emission lines are observed for the twinned areas, we believe that these crystal defects are perturbing f−f transitions, resulting in increased intensity. Based on these results and our recent findings published in ref 16, the high amount of Pr in addition to the presence of defects in $PrNbO_4$ makes these particles excellent luminescent materials. Moreover, we showed with our multitechnique approach that higher density of the twins leads to the strongest luminescence brightness, and therefore they are better candidates to be used in optical applications.

4. CONCLUSION

BSE, CL, and TEM studies were performed on $PrNbO_4$ powder particles at an identical location. Crystal defects of $PrNbO_4$ are visualized and explained in detail. Twinning as a result of phase transformation during the synthesis of the particles was observed. Further analysis showed that the twins are coherent. Two types of particles with high density and less density of the twins were found. The effect of the defect density on the optical properties of $PrNbO_4$ was investigated. Emission lines acquired for both of the particles were compared. For all these regions, there is no shift in the peak positions; however, there is a noticeable change in the intensity of the emission lines. Twinned areas with higher density showed higher intensity in comparison to twin-free areas and the regions with less density of the twins. For the major emission lines associated with the $^3P_0$ to $^3H_4$ and $^3P_2$ to $^3F_4$, regardless of the density, the intensity was significantly higher.

■ ASSOCIATED CONTENT

ⓈSupporting Information

The Supporting Information is available free of charge at https://pubs.acs.org/doi/10.1021/acsaelm.2c00253.

Figures S1−S3 and Table S1 (PDF)

■ AUTHOR INFORMATION

Corresponding Author

Christina Scheu − Max-Planck-Institut für Eisenforschung GmbH, 40237 Düsseldorf, Germany; ● orcid.org/0000-0001-7916-1533; Email: scheu@mpie.de

Authors

Rasa Changizi − Max-Planck-Institut für Eisenforschung GmbH, 40237 Düsseldorf, Germany

Stefan Zaefferer − Max-Planck-Institut für Eisenforschung GmbH, 40237 Düsseldorf, Germany

Lamya Abdellaoui − Max-Planck-Institut für Eisenforschung GmbH, 40237 Düsseldorf, Germany

Complete contact information is available at:
https://pubs.acs.org/10.1021/acsaelm.2c00253

■ REFERENCES

(1) Dou, R.; Zhang, Q.; Gao, J.; Chen, Y.; Ding, S.; Peng, F.; Liu, W.; Sun, D. Rare-earth tantalates and niobates single crystals: Promising scintillators and laser materials. *Crystals* **2018**, *8* (2), 55.

(2) Haugsrud, R.; Norby, T. Proton conduction in rare-earth ortho-niobates and ortho-tantalates. *Nat. Mater.* **2006**, *5* (3), 193−196.

(3) Zhang, H.; Wang, Y.; Xie, L. Luminescent properties of Tb^{3+} activated $GdTaO_4$ with M and M′ type structure under UV−VUV excitation. *Journal of luminescence* **2010**, *130* (11), 2089−2092.

(4) Nico, C.; Monteiro, T.; Graça, M. P. F. Niobium oxides and niobates physical properties: Review and prospects. *Prog. Mater. Sci.* **2016**, *80*, 1−37.

(5) Tsunekawa, S.; Takei, H. Twinning structure of ferroelastic $LaNbO_4$ and $NdNbO_4$ crystals. *Physica status solidi (a)* **1978**, *50* (2), 695−702.

(6) Albino, M.; Veber, P.; Castel, E.; Velazquez, M.; Schenk, K.; Chapuis, G.; Lahaye, M.; Pechev, S.; Maglione, M.; Josse, M. Growth and Characterization of Centimeter-Sized $Ba_2LaFeNb_4O_{15}$ Crystals from High-Temperature Solution under a Controlled Atmosphere. *Eur. J. Inorg. Chem.* **2013**, *2013* (15), 2817−2825.

(7) Kim, D. W.; Kwon, D. K.; Yoon, S. H.; Hong, K. S. Microwave dielectric properties of rare-earth ortho-niobates with ferroelasticity. *J. Am. Ceram. Soc.* **2006**, *89* (12), 3861−3864.

(8) Kelly, P. M.; Wauchope, C. J. The origin of the domain structure in $LaNbO_4$. *Mater. Lett.* **1996**, *27* (1−2), 7−11.

(9) Mir, S. H.; Takasaki, Y.; Engel, E. R.; Takamizawa, S. Ferroelasticity in an organic crystal: a macroscopic and molecular level study. *Angew. Chem., Int. Ed.* **2017**, *56* (50), 15882−15885.

(10) Bhattacharya, K. *Microstructure of Martensite: Why It Forms and How It Gives Rise to the Shape-Memory Effect*; Oxford series on

Materials Modelling; Oxford University Press: 2003; Vol. 2, pp 1−208.

(11) Prytz, O.; Tafto, J. Accurate determination of domain boundary orientation in LaNbO₄. *Acta Mater.* **2005**, *53* (2), 297−302.

(12) Fulle, K.; McMillen, C. D.; Sanjeewa, L. D.; Kolis, J. W. Hydrothermal chemistry and growth of fergusonite-type RENbO₄ (RE = La−Lu, Y) single crystals and new niobate hydroxides. *Cryst. Growth Des.* **2016**, *16* (9), 4910−4917.

(13) Jian, L.; Wayman, C. M. Electron back scattering study of domain structure in monoclinic phase of a rare-earth orthoniobate LaNbO₄. *Acta metallurgica et materialia* **1995**, *43* (10), 3893−3901.

(14) Brixner, L. H.; Whitney, J. F.; Zumsteg, F. C.; Jones, G. A. Ferroelasticity in the LnNbO₄-type rare earth niobates. *Mater. Res. Bull.* **1977**, *12* (1), 17−24.

(15) Rojas-Gonzalez, F. E.; Hernandez-Negrete, O.; Esparza-Ponce, H. E.; Hernandez-Paredes, J. A method to decorate the surface of LiNbO₃: Eu³⁺ powders with EuNbO₄ nanoparticles. *J. Alloys Compd.* **2020**, *830*, 154688.

(16) Changizi, R.; Zhang, S.; Ziegler, C.; Schwarz, T.; Lotsch, B. V.; Scheu, C. Correlation between Structural Studies and the Cathodoluminescence of Individual Complex Niobate Particles. *ACS Applied Electronic Materials* **2021**, *3* (1), 461−467.

(17) Uma, S.; Gopalakrishnan, J. K₁₋ₓLaₓCa₂₋ₓNb₃O₁₀, a layered perovskite series with variable interlayer cation density, and LaCaNb₃O₁₀, a novel layered perovskite oxide with no interlayer cations. *J. Solid State Chem.* **1993**, *102* (2), 332−339.

(18) Frank, A.; Changizi, R.; Scheu, C. Challenges in TEM sample preparation of solvothermally grown CuInS₂ films. *Micron* **2018**, *109*, 1−10.

(19) Marfunin, A. S. *Composition, Structure, and Properties of Mineral Matter: Concepts, Results, and Problems*; Springer: 1994.

(20) Dieke, G. H.; Crosswhite, H. M. The spectra of the doubly and triply ionized rare earths. *Applied optics* **1963**, *2* (7), 675−686.

(21) Cybińska, J.; Legendziewicz, J.; Boulon, G.; Bensalah, A.; Meyer, G. Assignment of spectroscopic properties in praseodymium-doped and praseodymium/ytterbium-co-doped ternary K₂LaX₅ (X= Cl, Br, I) Halides. *Opt. Mater.* **2006**, *28* (1−2), 41−52.

(22) Li, Y. C.; Chang, Y. H.; Lin, Y. F.; Chang, Y. S.; Lin, Y. J. Luminescent properties of trivalent praseodymium-doped lanthanum aluminum germanate LaAlGe₂O₇. *J. Phys. Chem. Solids* **2007**, *68* (10), 1940−1945.

(23) Kumar, M. K.; Parandamaiah, M.; Babu, Y. N.; Kumar, A. Spectral studies of praseodymium doped heavy metal borate glass systems. *Int. J. Eng. Sci.* **2014**, 17−24.

(24) Ji, Y.; Cao, J.; Zhu, Z.; Li, J.; Wang, Y.; Tu, C. Luminescence properties and white emission in Pr³⁺ doped hexagonal YAlO₃ nanophosphors. *Materials Express* **2011**, *1* (3), 231−236.

(25) Feng, W.; Lin, H.; Liu, H. Photoluminescence and crystal-field analysis of Pr³⁺-doped SrMoO₄ phosphors. *Zeitschrift für Naturforschung A* **2015**, *70* (1), 11−16.

(26) Li, Y.; Yu, Q.; Huang, L.; Wang, J.; Su, Q. Near ultraviolet and visible-to-near-infrared spectral converting properties and energy transfer mechanism of Sr₂SiO₄: Ce³⁺, Pr³⁺ phosphor. *Optical Materials Express* **2014**, *4* (2), 227−233.

(27) Hatanaka, M.; Yabushita, S. Theoretical study on the f−f transition intensities of lanthanide trihalide systems. *J. Phys. Chem. A* **2009**, *113* (45), 12615−12625.

(28) Hatanaka, M.; Yabushita, S. Mechanisms of f−f hypersensitive transition intensities of lanthanide trihalide molecules: a spin−orbit configuration interaction study; Springer: 2016; pp 219−233.

(29) Lima, A. R. F.; Sczancoski, J. C.; Li, M. S.; Longo, E.; Camargo, E. R. Structural characterization and photoluminescence behavior of pure and doped potassium strontium niobates ceramics with tetragonal tungsten−bronze structure. *Ceram. Int.* **2016**, *42* (4), 4709−4714.

(30) Morais, B.; Foot, P. J. S.; Kresinski, R. A. Synthesis and photoluminescent properties of Sm³⁺-doped SnO₂ nanoparticles. *Ceram. Int.* **2016**, *42* (16), 18474−18478.

(31) Bouras, K.; Rehspringer, J. L.; Schmerber, G.; Rinnert, H.; Colis, S.; Ferblantier, G.; Balestrieri, M.; Ihiawakrim, D.; Dinia, A.; Slaoui, A. Optical and structural properties of Nd doped SnO₂ powder fabricated by the sol-gel method. *J. Mater. Chem. C* **2014**, *2* (39), 8235−8243.

(32) van Hest, J. J. H. A.; Blab, G. A.; Gerritsen, H. C.; de Mello Donega, C.; Meijerink, A. Probing the influence of disorder on lanthanide luminescence using Eu-doped LaPO₄ nanoparticles. *J. Phys. Chem. C* **2017**, *121* (35), 19373−19382.